Influence of copper-coated graphene films on mechanical and damping properties of bionic laminar CuAlMn matrix composites

Dongxuan Li [a,b], Xiaosong Jiang [a,b,*], Hongliang Sun [a,b], Zixuan Wu [c], Liu Yang [d]

[a] Key Laboratory of Advanced Technologies of Materials, Ministry of Education, Chengdu, 610031, China
[b] School of Materials Science and Engineering, Southwest Jiaotong University, Chengdu, Sichuan, 610031, China
[c] School of Engineering and Materials Science, Queen Mary University of London, London, E1 4NS, United Kingdom
[d] Institute for Applied Materials (IAM-WK), Karlsruhe Institute of Technology (KIT), Karlsruhe, 76131, Germany

ARTICLE INFO

ABSTRACT

Inspired by the structure of nacre, bionic laminar composites composed of 85.6 wt% Cu, 11.9 wt% Al, and 2.5 wt% Mn were prepared using highly flexible Cu-coated graphene films as fillers. The effects of surface modification and graphene films content on the properties were investigated. Results indicated that the loss factor of composites with 0.1 wt% Cu-coated graphene films is improved by approximately 28% and reaches 0.044 compared to uncoated samples. The density and tensile strength are increased by up to 98% and 362 MPa, respectively. This enhancement is attributed to the improved bonding at the graphene films/matrix interface due to the Cu coating, which allows for efficient load transfer. Concurrently, the activation of interlayer sliding in the graphene films dissipates substantial energy. However, an excessive addition of graphene films leads to decreased density and increased internal defects in the composites, resulting in deteriorated properties. This study provides a reference for the preparation of CuAlMn matrix composites with enhanced mechanical and damping properties.

1. Introduction

CuAlMn alloys have been widely researched as high-damping materials, with current studies focusing on the addition of alloying elements [1], reinforcements [2], and heat treatment [3] to enhance their damping properties. However, enhancing damping properties often leads to a decrease in the strength. The nacre in nature excellently combines static (stiffness and toughness) and dynamic (damping) mechanical properties [4]. Its interlocking "brick-mortar" structure facilitates energy dissipation [5,6], while intrinsic and extrinsic toughening mechanisms enable excellent mechanical properties [7]. Inspired by nacre, constructing laminar structures is an effective method to enhance both the strength and damping properties of CuAlMn matrix composites, and the selection of suitable filler as "mortar" is crucial in this preparation [6].

The "mortar" in nacre refers to soft and ductile fillers [8] that allow for slight movement of the surrounding hard mineral sheets to relieve stress concentrations [9]. Graphite exhibits excellent self-lubricating properties, making it an ideal choice as a filler. Recently, a variety of two-dimensional carbon materials have been developed from graphite, including graphene and graphene films (GFs) [10,11]. GFs are flaky

carbon materials assembled from stacks of graphene [12–15]. Their larger size enhances orientation controllability [16], while the internal micro-fold structure provides GFs with excellent flexibility and ductility [17]. Compared to graphene, GFs not only possess excellent mechanical properties but also superior damping properties [18]. Monolayer graphene lacks intrinsic damping capability, with its damping contribution arising solely from friction and sliding at the interface with the matrix [19]. In contrast, multilayer graphene exhibits three energy dissipation mechanisms: sliding, rippling, and impacts [20]. Among these, interlayer sliding serves as the predominant mode of energy dissipation because the weak van der Waals bonds between graphene layers break easily [21]. Additionally, the micro-fold structure in GFs plays a crucial role in energy dissipation as well [22].

However, directly incorporating graphene into the CuAlMn matrix tends to cause agglomeration and can only form interfaces for mechanical interlocking [23]. Weak interfacial bonding significantly reduces the strengthening effect [24]. Commonly used dispersion methods, such as high-energy ball milling and organic solution dispersion, often damage the structure of graphene and compromise its wettability with the metal matrix [25,26]. In contrast, using electroless plating to coat metal layer on the surface of GFs effectively addresses

these issues [27]. This technique does not damage GFs and provides advantages such as controllable deposition thickness and densified microstructure [28–32]. It improves the dispersion of reinforcements and the wettability between GFs and metal matrix, thereby enhancing the interfacial bond strength [33]. Montazeri et al. [34] used molecular dynamics simulation to investigate the effect of graphene surface coating on load transfer in Cu-matrix nanocomposites, finding that the coating significantly improved the shear stress at the interface when graphene was pulled out. Wang et al. [35] conducted simulations to assess the effects of Ni, Cu, and Ti coatings on the interfacial bonding and mechanical properties of Al-matrix composites, demonstrating that these coatings enhanced Young's modulus and microhardness.

In this work, bionic laminar 85.6 Cu-11.9 Al-2.5 Mn (wt.%) composites were fabricated via flake powder metallurgy. GFs were used as reinforcements and Cu particles encapsulated on GFs (referred to as GFs (Cu)) through electroless plating. Scanning electron microscopy (SEM) and transmission electron microscopy (TEM) were employed to characterize the interfaces and microstructures of the composites. The tensile strength and damping properties of the composites were evaluated, and a comparative analysis was proceeded to assess the effects of Cu coating and GFs content on the properties. Additionally, the mechanisms of interfacial bonding on mechanical and damping properties were explored, providing new insights into the development of composites with both high mechanical and damping properties.

2. Experimental

2.1. Material preparation

The raw materials for the experiments included Cu powder (250 mesh), Al powder (300 mesh), Mn powder (300 mesh) and GFs (density approximately 2 g/cm^3, thickness around 12 μm). GFs were roughened by immersion in a roughing solution (HCl + Ethanol) using ultrasound. Subsequently, the films underwent sequential treatment with a sensitizing solution (SnCl$_2$ + HCl) followed by an activation solution (PdCl$_2$ + HCl). The treated GFs were then immersed in a plating solution composed of CuSO$_4$·5H$_2$O (15 g/L), C$_4$O$_6$H$_4$KNa (14 g/L), EDTA (14 g/L), and water. The solution was stirred with a magnetic stirrer, and NaOH was used to adjust the pH to 12.5–13, while formaldehyde served as a reducing agent to facilitate copper precipitation. The plating solution was filtered off by stirring for about 20 min, then copper-coated graphene films (GFs(Cu)) were removed and dried in an oven for 24 h.

In order to achieve the flake morphology, Cu and Al powders were ball milled at 300 rpm for 6 h and 3 h, respectively. Subsequently, 0.1 wt % GFs, 0.1 wt% GFs(Cu), 0.2 wt% GFs(Cu), and 0.3 wt% GFs(Cu) were selected and mixed with metal powders for 1 h, followed by drying using a vacuum freeze dryer. Dense metal blocks were obtained by sintering at 27 MPa and 850 °C using vacuum hot pressing. The experimental flow is shown in Fig. 1.

2.2. Material characterization

The morphology and chemical composition of the composite powders and GFs(Cu) were analyzed using scanning electron microscopy (SEM, ZEISS Sigma 300) and energy dispersive spectroscopy (EDS). Phase compositions of the composites were determined using an X-ray diffractometer (XRD, Rigaku XRD-6100). Microscopic morphology and phase distribution of sample cross sections were initially observed by SEM, and the phase morphology and interfacial bonding were further analyzed using transmission electron microscopy (TEM, FEI Talos F200X). Tensile strength was measured by utilizing a universal testing machine (WDW-3100) at a speed of 0.5 mm/min, and fracture morphology was observed using SEM. Damping properties of the samples at room temperature were tested with a Dynamic Mechanical Analyzer (DMA, TA DMA850) at a frequency of 1 Hz and an amplitude range of 1–500 μm.

3. Results and discussion

3.1. Microstructures of Cu-coated graphene films and composite powders

Electroless plating faces the challenge of poor wettability between Cu and GFs, necessitating a pretreatment process (roughening-sensitizing-activating) to enhance the adhesion of Cu particle. The initial roughening of GFs provides more attachment points for Cu particles during subsequent electroless plating, thereby enhancing the boundary between Cu coating and GFs [36]. Sensitization and activation treatments reduce Sn^{2+} to obtain Pd, which serves as an activation center for catalytic reaction and facilitates the uniform distribution of Cu particles [37]. The reactions involved are shown in equations (1)–(4).
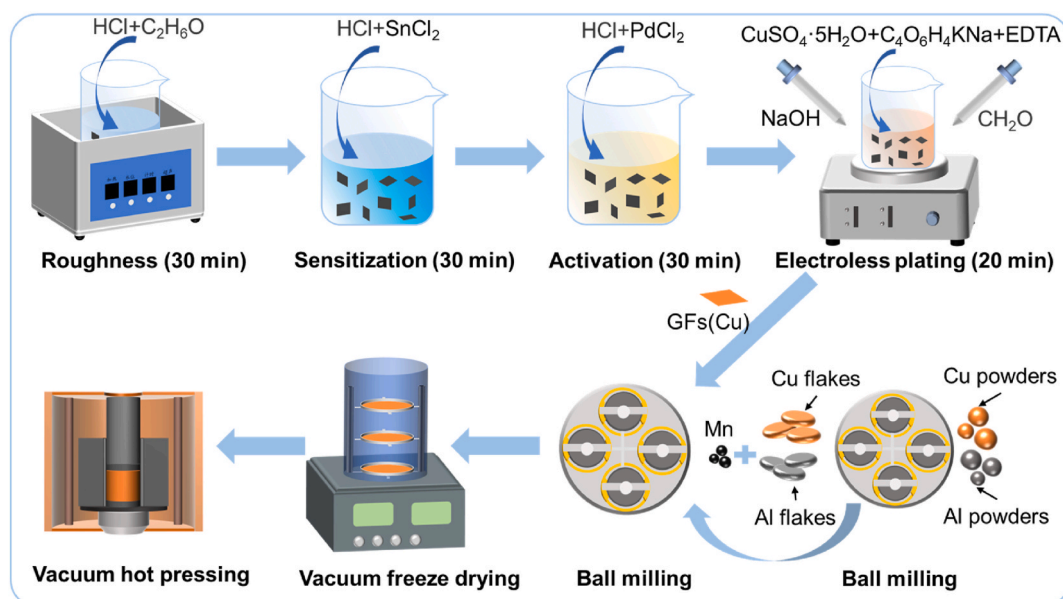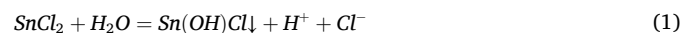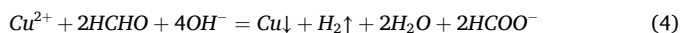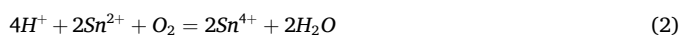
$$SnCl_2 + H_2O = Sn(OH)Cl\downarrow + H^+ + Cl^- \tag{1}$$

Fig. 1. Schematic diagram of the preparation process of GFs(Cu)/CuAlMn laminated composites.

$$4H^+ + 2Sn^{2+} + O_2 = 2Sn^{4+} + 2H_2O \tag{2}$$

$$Sn^{2+} + Pd^{2+} = Sn^{4+} + Pd \tag{3}$$

$$Cu^{2+} + 2HCHO + 4OH^- = Cu\downarrow + H_2\uparrow + 2H_2O + 2HCOO^- \tag{4}$$

During electroless plating, temperature, time, and pH significantly influence the coating quality. Previous investigations have indicated that optimal results are achieved by stirring GFs in the plating solution at pH 12.5 and 45 °C for approximately 20 min [37]. Fig. 2a and b depict the surfaces that are incompletely covered due to excessively temperatures, resulting in uneven Cu particle deposition. In contrast, Fig. 2c and d illustrate the successful attachment of Cu particles to the GFs surface, with the magnified image demonstrating a relatively uniform and densified coating that shows no apparent delamination or cracks. Fig. 2e and f shows that the coating consists entirely of copper with no signs of contamination by impurities.

Microscopic morphology of the composite powders is shown in Fig. 3. Fig. 3a and b reveal that Cu and Al powders predominantly exhibit a flaky morphology, while Mn powders have an irregular shape. Al flakes generally exhibit a circular shape, with a maximum diameter of 88 μm and an average size of 38 μm. In contrast, Cu flakes display an irregular morphology with significant size variations, ranging from 10 to 39 μm in diameter and the average size is 19 μm. The sizes of Cu and Al flakes, serving as "bricks" for laminate structure, affecting the layer morphology and properties of the composites [6]. EDS results (Fig. 3c–f) indicate a uniform mixing of the powders. The protective effect of the ball milling medium (*tert*-butyl alcohol) minimizes cold-welded particles, resulting in good dispersion.

3.2. Microstructures and characterization of composites

Phases were identified using X-ray diffraction (XRD), with the results presented in Fig. 4. The CuAlMn alloy undergoes a eutectoid reaction during furnace cooling, leading to the formation of α and γ2 phases [38]. The presence of Mn inhibits the eutectoid reaction, resulting in the retention of some parent phases and the formation of two types of martensite (β_1' and γ_1') [39]. However, the amount of martensite is relatively low. SEM images (Fig. 5) clearly show GFs distribution with some orientation, but no diffraction peak of carbon was detected in the XRD pattern, probably due to the low content of GFs.

Fig. 5a, b, d, and e display the micro-morphology of cross-sections with varying GFs contents. The GFs exhibit a black stripe morphology that is predominantly oriented perpendicular to the pressurization direction. This regular orientation is partly a result of gravitational self-assembly during the hot-pressing process and is influenced by the morphology of powders. Flake powders demonstrate good morphological compatibility with GFs, enhancing their dispersion and alignment during ball milling and hot pressing [40]. Elemental distribution of the sample containing 0.1 wt% GFs (Cu) is shown in Fig. 5c, indicating that black areas represent GFs, which are tightly bonded to the matrix with no observable pores at the interface. The absence of a distinct Cu coating around GFs can be attributed to good compatibility between the Cu coating and matrix [32]. Fig. 5f illustrates the phase morphology and distribution, with elemental compositions detailed in Table 1. The light-colored region represents the α-phase (region 1), a solid solution formed after a small amount of Al enters the Cu lattice. In contrast, the dark-colored region corresponds to γ2-phase (region 3), which is a solid solution based on intermetallic compounds [41]. Mn inhibits the
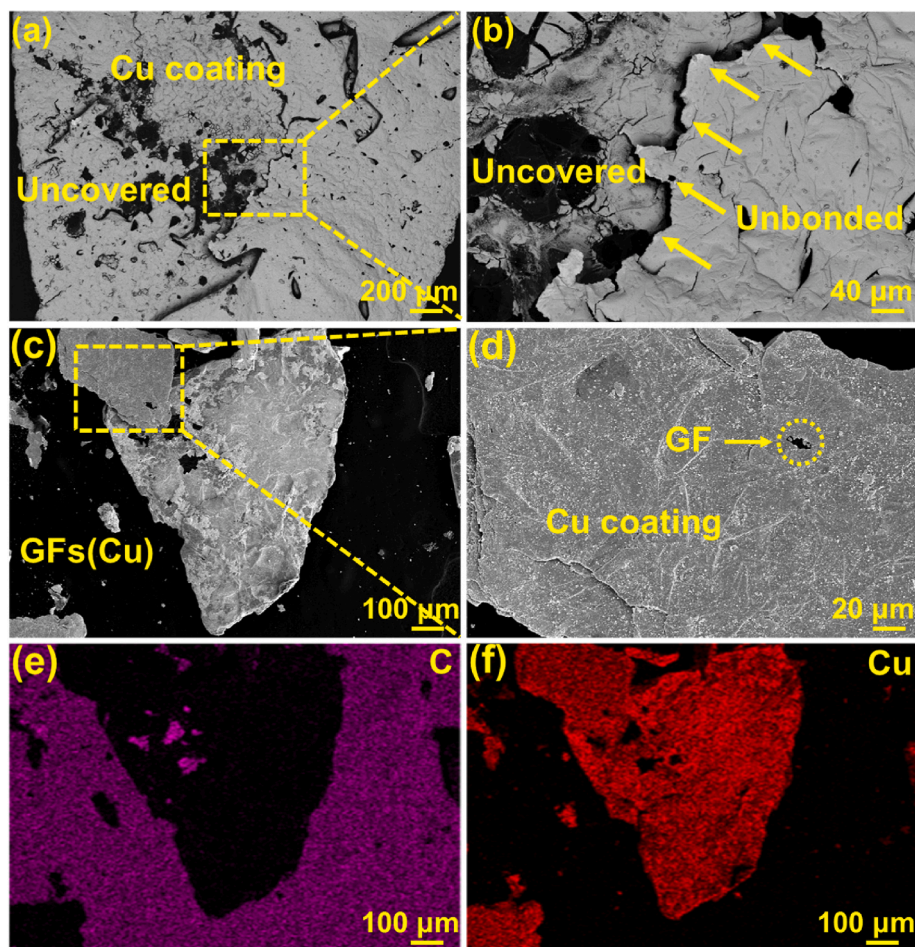

Fig. 2. SEM images of GFs surface: (a, b) electroless plating at 75 °C for 20 min, (c, d) electroless plating at 45 °C for 20 min, (e, f) EDS results of (c).
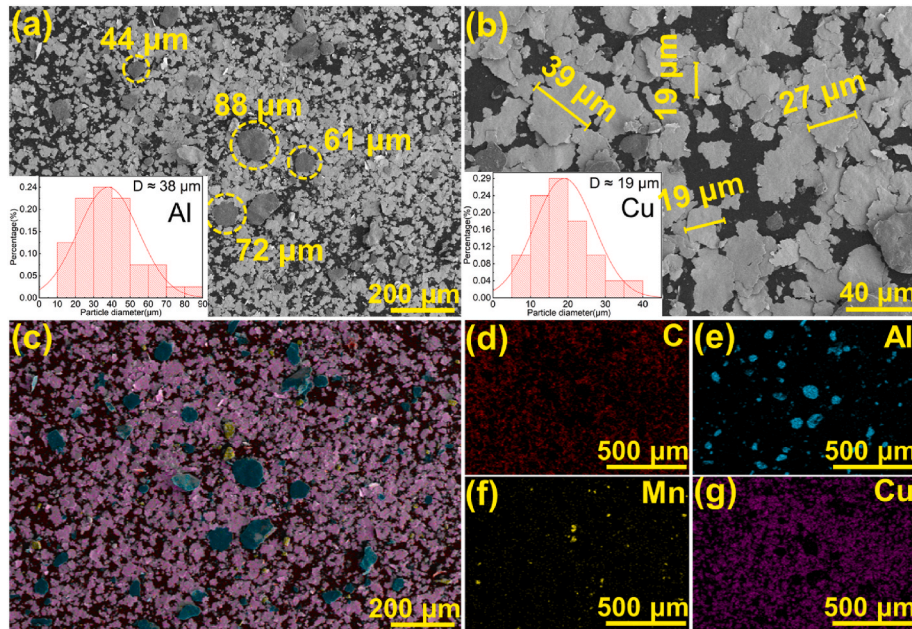
Fig. 3. SEM results of composite powders: (a, b) micro-morphology of Al and Cu particles in the composite powders as well as average size statistics, (c–g) EDS results of (a).
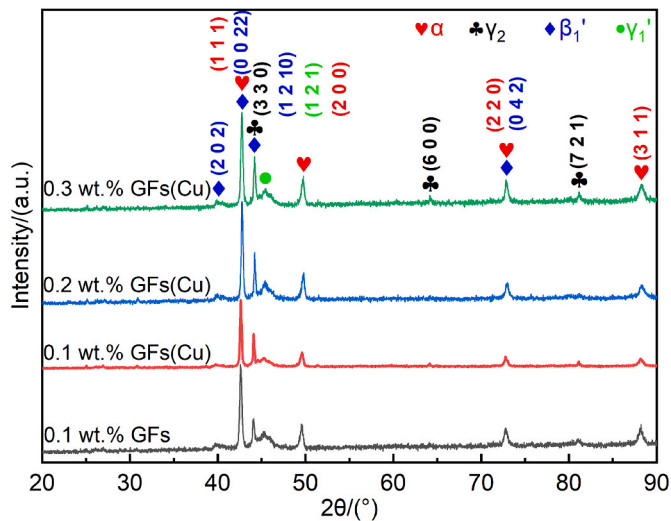

Fig. 4. XRD patterns of the composites with different GFs contents.

eutectoid reaction, allowing the retention of a small amount of parent phase, which subsequently forms martensite (region 2). Additionally, a black region devoid of GFs was observed (region 4), and EDS results indicate that a small amount of oxide has formed in this area.

Fig. 6a presents a TEM image of the matrix, revealing two main phases. Electron diffraction analysis indicates that the a_2 region corresponds to the α-Cu phase, which exhibits a FCC structure. In contrast, the a_1 region represents the $γ_2$ phase, which is characterized by a BCC structure and higher concentration of Al. A small number of particles enriched in Al and O were observed at the grain boundaries in Fig. 6c and e, indicating the formation of a small amount of aluminum oxide. A significant area of martensite appears in Fig. 6g, predominantly exhibiting in a lath-like structure. Its inner twin structure becomes visible upon magnification in Fig. 6h. The high-resolution TEM image of the twin boundary and the selected area electron diffraction (SAED) results are shown in Fig. 6i. Based on the SAED pattern, this region can be identified as $2H(γ_1')$ martensite. Twinning occurs in martensite with

$(12\bar{1})$ plane, which serves as twin plane and is observed in [101] direction, classified as type I twinning [42]. High-resolution TEM images reveal clear, straight, parallel twin boundaries, with stacking faults appearing around these boundaries, which manifest as streaks parallel to the $(12\bar{1})$ crystal plane in the SAED diagram. The phase composition in the matrix is closely related to Al content. During the eutectoid reaction, Al atoms diffuse to grain boundaries and forms Al-rich $γ_2$ phase, while Al-poor regions transform into the α-Cu phase. Regions with high Al content are more likely to form $2H(γ_1')$ martensite during the martensitic transformation. To accommodate the strain generated during the thermoelastic martensite formation, parallel or V-shaped adaptive structures form within the martensite [39], as shown in Fig. 6g.

Fig. 7 demonstrates the TEM morphology of the 0.1 wt% GFs(Cu) composite, highlighting two selected regions for the characterization of GFs. The bright-field TEM image shown in Fig. 7a reveals that white areas in the form of bars and granules within the matrix. Element mapping results indicate that these bars consist of curved GFs, with notable aluminum oxides observed between and around the GFs. The formation of oxides may be attributed to the introduction of O during ball milling and electroless plating process. Fig. 7g displays GFs embedded within the α-Cu phase, with SAED patterns for both the α phase and GFs shown in Fig. 7i$_1$. Fig. 7h and i provide high-resolution TEM images at the interface where GFs bond to the matrix. These images reveal an amorphous structure with circular SAED pattern, as shown in Fig. 7i$_1$.

Fig. 7j presents a high-resolution TEM image of the GFs, revealing a continuous and uniform strip with a thickness of approximately 13.3 nm. Internal crystal planes exhibit ordered arrangement, with SAED patterns revealing the (002) and (004) crystal planes of the GFs, and crystal plane spacing measured at approximately 0.35 nm. There is a transition region between the GFs and the matrix, with a width of 6–7 nm, while the end transition region is narrower at only 2.5 nm. The inverse fast Fourier transform (Fig. 7j, upper right) clearly reveals a significant number of dislocations in the transition region around interface. This formation is attributed to the substantial differences in thermal expansion coefficients between the GFs and the matrix, which generate an internal stress at the interface during temperature fluctuations [3]. In order to alleviate thermal mismatch strain, a high-density dislocation zone develops around the GFs. Furthermore, the GFs
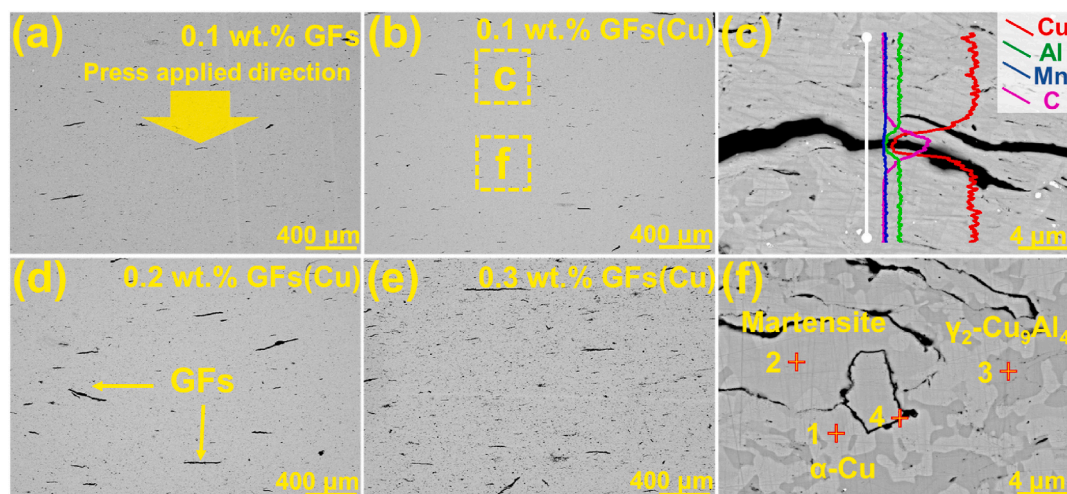
Fig. 5. (a, b, d, e) SEM images of the composites with different GFs contents, (c, f) enlarged SEM images of the composite with 0.1 wt% GFs(Cu) content.

Table 1
Distribution of selected elements in different regions.

	1	2	3	4
Cu (at.%)	63.28	61.21	58.04	37.03
Al (at.%)	16.36	20.03	24.13	24.33
O (at.%)	1.19	1.03	0.92	26.74

impede dislocation movement, leading to the accumulation and entanglement of dislocations in the interfacial region, which ultimately enhances the mechanical properties of the composites.

3.3. Mechanical properties of composites

The density of the composites was measured using the Archimedes drainage method, the results are shown in Fig. 8a. The relative density of the composite with 0.1 wt% GFs is 0.974, which increased to 0.982 after the application of Cu coating on GFs surface. This increase indicates that the Cu coating enhances interfacial bonding between the GFs and the matrix while reducing the porosity of the composites. As the content of GFs increases, the pore volume within the composites also rises, leading to a gradual decrease in density.

Tensile strength was evaluated along the laminar direction using a universal testing machine, with the stress-strain curve depicted in Fig. 8b. The ultimate tensile strength of the uncoated composites was about 338 MPa. However, the application of Cu coating improved the mechanical properties of the composites, increasing the ultimate tensile strength to 362 MPa and strain to approximately 19%. These enhancements result from the improved interfacial bonding, reduced internal porosity, and more effective load transfer induced by the Cu coating [34].

Furthermore, neatly arranged GFs create laminated structure with the matrix, while highly flexible GFs enable micro-sliding between layers of metal sheets, alleviating stress concentration and preventing premature crack formation. Once cracking occurs, GFs can alter the crack propagation path, thereby improving toughness. However, composite mechanical properties decreased with the increase of GFs content, the ultimate tensile strength and strain decreased to 286 MPa and 13%, respectively. This decline is attributed to decreased dispersion due to higher GFs content, along with the increase in pores and weak points within the material, resulting in diminished tensile strength.

The fracture characteristic was analyzed to elucidate the mechanisms for changes in strength, and the morphology is presented in Fig. 8c–f. There are mainly two types of dimples and cleavage in the matrix (Fig. 8e), showing a mixed fracture mode exhibiting both toughness and brittleness. Fig. 8c shows several long, deep cracks in the composite without Cu coating, with GFs visibly separated from the matrix within these cracks. This observation implies poor bonding between GFs and the matrix, resulting in reinforcement debonding and subsequent crack formation during tensile testing [43]. In contrast, as shown in Fig. 8d, the depth of transverse cracks in Cu-coated composite is shallower, and no thicker GFs are present. This change suggests that the Cu coating enhances both the dispersion of GFs and their bonding with the matrix, allowing GFs to remain attached during fracture and effectively facilitate load transfer. Fig. 8e and f depict long, continuous GFs with some delamination at the interface, indicating that bonding remains inadequate. Micro-folds on the GF surface are visible in the magnified image [44], which can inhibit the densification of GFs, leading to the reduction in the density of the composite [10]. Additionally, the larger size of GFs may accelerate crack propagation along the interface, reducing material strength and ductility.

During the hot pressing process, uncoated GFs form weak mechanical bonds with the metal matrix, primarily connecting through friction generated by surface roughness [33]. As shown in Fig. 8c, large gaps appear at both the upper left and right sides of the fracture, indicating weak bonding between the GFs and matrix. Generally, mismatches in thermal expansion coefficients between reinforcement and metal matrix [24] lead to the formation of high-density dislocation zone around the interface. For weak interfaces, dislocation accumulation around the interface may lead to stress concentration, preventing the composite from achieving its desired properties [45]. The densified Cu coating on GFs creates an "interlocking effect", binding GFs and metal matrix tightly [32]. This interaction in the interfacial region significantly influences load transfer capacity and enhances the interfacial shear strength [46]. The observation of the fracture morphology in Fig. 8d shows that GFs remain tightly connected to the matrix. This strong interfacial bonding prevents premature crack formation, allowing GFs to absorb more energy during fracture, thus increasing the material's strength [34]. The reinforcement mechanism is illustrated in Fig. 9.

3.4. Damping properties of composites

The damping properties of the composites were tested at room temperature to obtain curves of damping values, loss modulus, and storage modulus as functions of amplitude. Fig. 10 presents the damping strain curves, with the vertical coordinate tan δ, referred to as the loss factor. This factor represents the ratio of loss modulus to storage modulus, reflecting the viscoelasticity of the material and characterizing damping capacity. The data indicate that the value continues to increase with the rise in strain amplitude. This phenomenon occurs because the
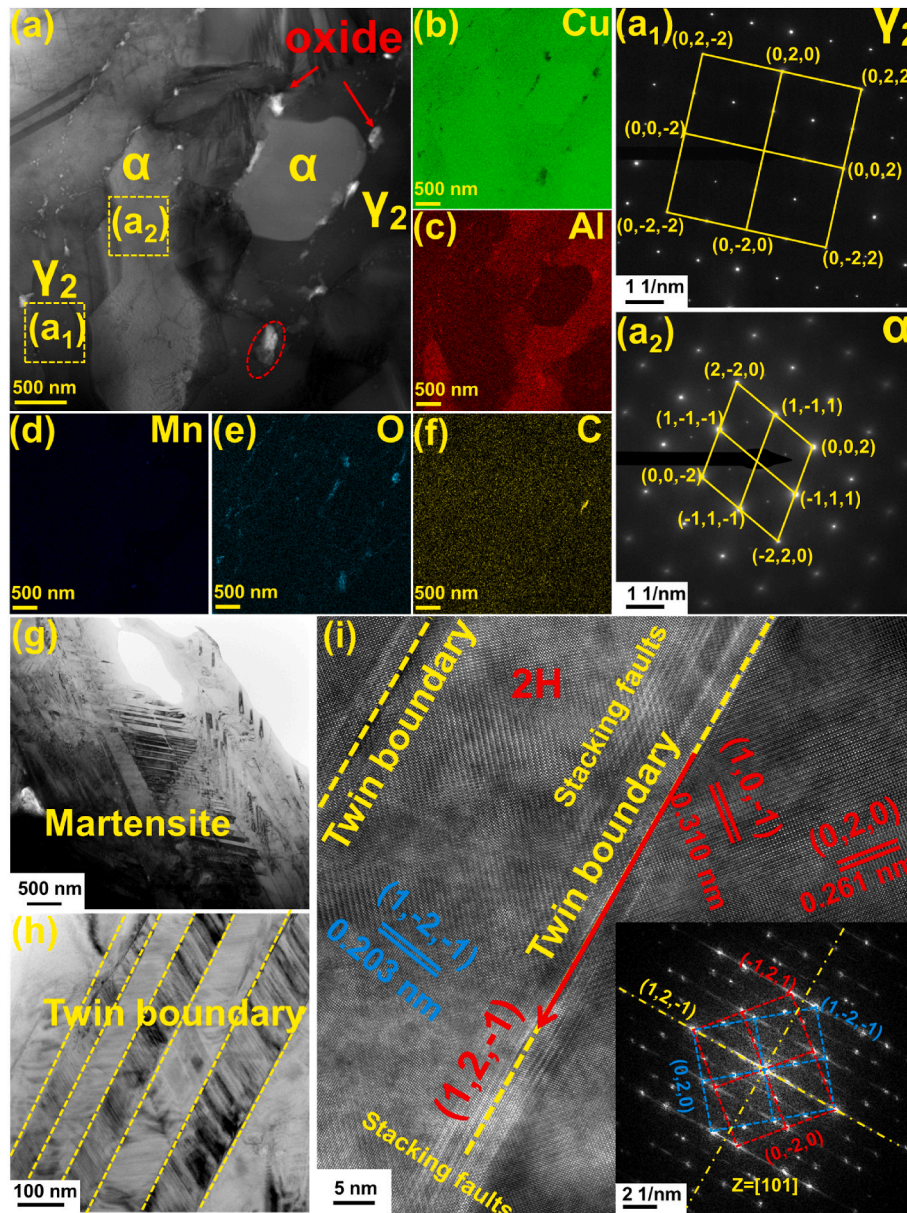
Fig. 6. (a–f) TEM images and elemental distribution of α and γ₂ phases, (a₁, a₂) selected area electron diffraction images of α and γ₂ phases, (g–h) TEM images of martensite, (i) high-resolution transmission electron microscopy and selected area electron diffraction images of twins in 2H martensite.

energy dissipation is caused by internal dislocation movement, viscous movement at the martensite/matrix interface and sliding friction between GFs and the matrix. As strain amplitude increases, these mechanisms exacerbate energy dissipation, leading to a higher tan δ value.

At low strains and room temperature, grain and phase boundaries are difficult to move, making dislocation movement the primary mechanism contributing to damping properties [47]. According to G-L theory [48], dislocations within the material are anchored between strong pinning points (e.g., grain boundaries or precipitation phases) and weak pinning points (e.g., vacancies), as shown in Fig. 11. When the external force is small, dislocations oscillate between weakly pinned points. As force increases, dislocations detach from these weak points and oscillate between strongly pinned points, resulting in higher energy dissipation. An increased strain amplitude activates more movable dislocations, enhancing both their quantity and mobility [49], thereby improving damping ability at low strain amplitudes. Samples with 0.1 wt% GFs exhibit relatively high tan δ values, but these values decrease after Cu coating. The significant difference in coefficients of thermal expansion

between GFs and matrix [3] generates residual stresses at the interface, causing the matrix to undergo plastic deformation and increasing dislocation density. The coefficient of thermal expansion of Cu coating is similar to that of the matrix, which reduces mismatch strain on one side and decreases the dislocation density, thus weakening the damping effect [50].

The tan δ value rises with increasing strain amplitude, but the curve gradually flattens. This behavior may occur because the number of movable dislocations has reached saturation and no longer increases with amplitude. Most dislocations move out of weak pinning points, resulting in limited increase in energy dissipation capacity [51]. Additionally, the increased dislocation number and mobility after amplitude rising may lead to interactions that form dislocation entanglements, increasing the number of strong pinning points. This limits dislocation movement range, which is unfavorable for damping properties, making dislocation movement less significant at high amplitudes. As strain amplitude rises, the GFs/matrix interface starts contributing to damping, causing further increase in tan δ value. The curve for the 0.1 wt%
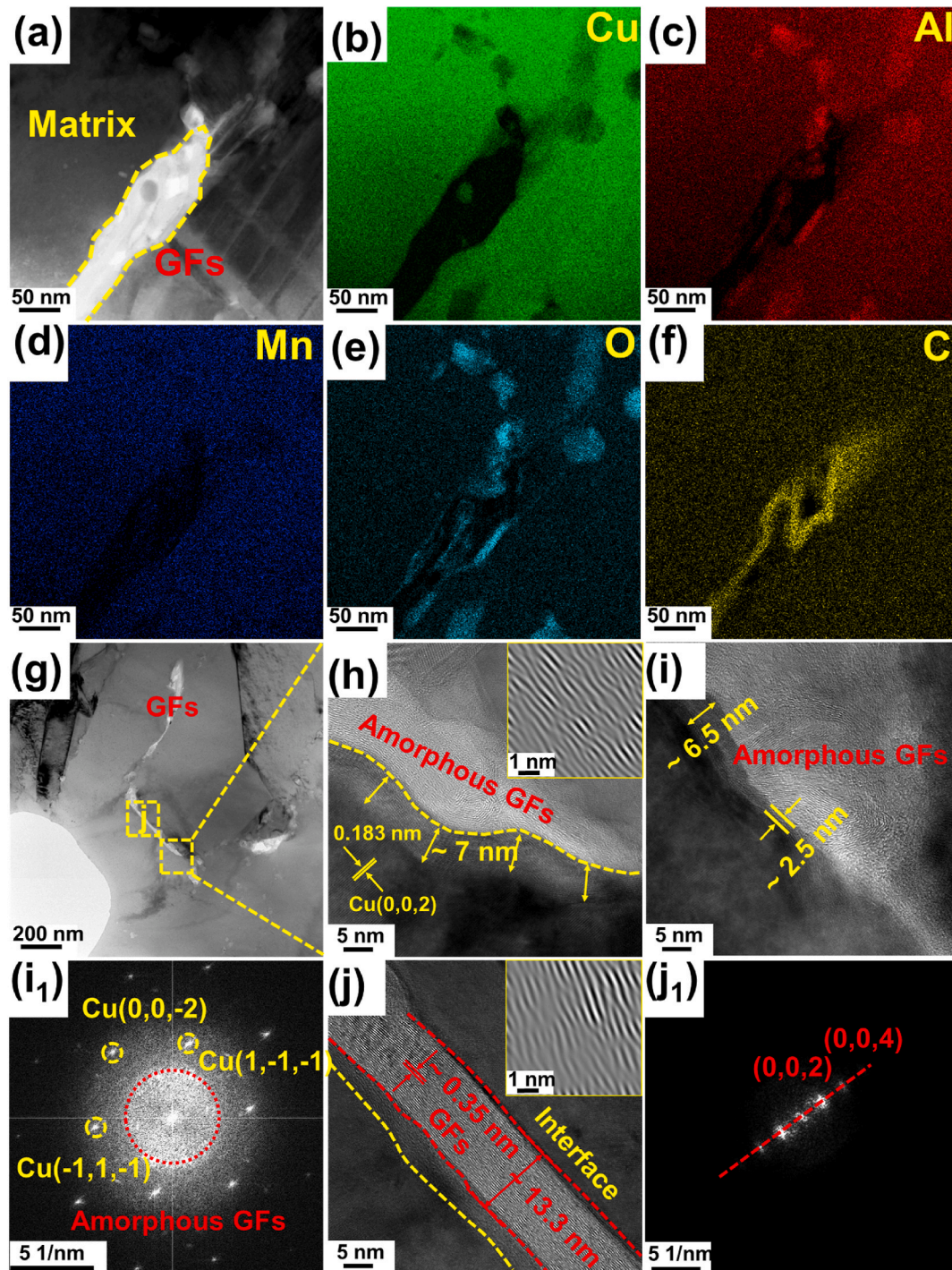
Fig. 7. (a–f) TEM images and elemental distribution of graphene films, (g–j) TEM, high-resolution transmission electron microscopy and selected area electron diffraction images of graphene films/matrix interface.

GFs(Cu) sample displays a higher slope different from others. Its tan δ value surpasses that of the 0.1 wt% GFs sample at a certain point and gradually widens the gap with other samples, reaching a maximum of about 0.045. In contrast, the uncoated sample has a maximum tan δ value around 0.035, while increasing GFs content significantly reduces the tan δ value to around 0.029, which is even lower than that of the 0.1 wt% GFs sample.

The interfacial damping mechanism is illustrated in Fig. 12. Various interfaces exist in the composite, including phase and twin boundaries, as shown in Fig. 6. The bonding between GFs and the matrix is relatively weak, making it susceptible to sliding friction as strain amplitude

increases. Additionally, the large size of the GFs and their incoherence with the matrix lead to stress concentration at the interface (particularly at end of GFs), and dislocation accumulate towards this region. The self-lubricating effect of the GFs allows the interface to deform or slide, thereby reducing stress concentration [52]. Weak interfacial bonding results in inefficient shear load transfer to GFs, leading to slip primarily occurring at the GFs/matrix interface. The Cu coating significantly improves the interfacial bonding between GFs and the matrix, allowing effective stress transfer to graphene interlayers and activating slip between these layers. Multilayer graphene layers bond through weak van der Waals forces, making the interfaces more prone to slip under cyclic
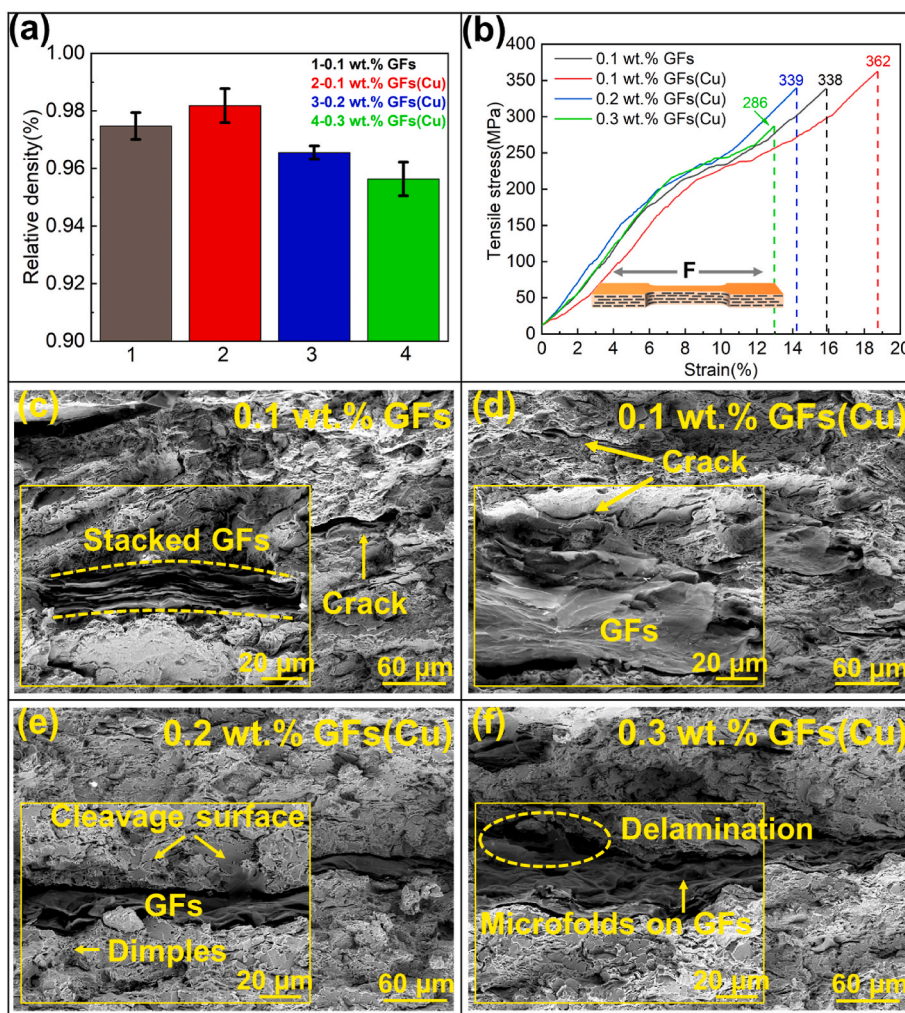
Fig. 8. (a, b) Relative density and engineering stress-strain curves of the composites, (c–f) fracture morphology of the composites.
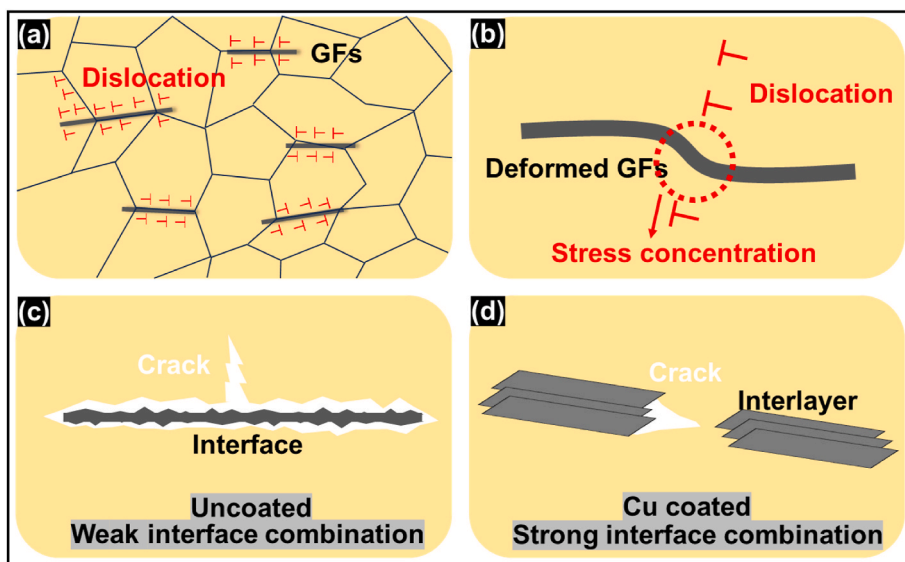

Fig. 9. (a, b) Dislocations around graphene films and interaction between graphene films and dislocations, (c) Cracks form at weak interfaces, (d) Cracks form between layers of graphene films.
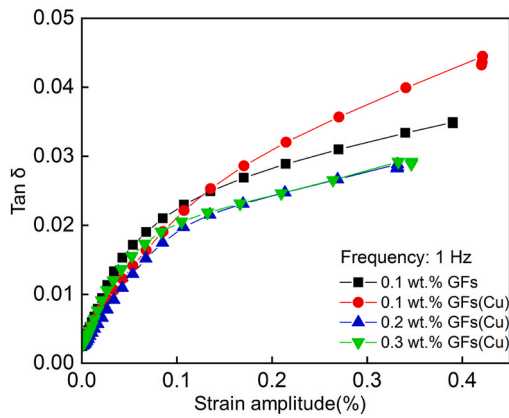
Fig. 10. Damping strain curves of composites.

loading, which leads to significant energy dissipation. The superposition of graphene interfacial and interlayer slip greatly enhances the damping properties [53]. A schematic representation of interfacial damping appears in Fig. 12. Furthermore, the "interlocking effect" generated by the coating results in interface sliding friction that exceeds that of the uncoated state. Energy dissipation from interfacial slip can be expressed by the following equation [54].

$$\Delta U = \int \delta l \cdot f \cdot dS \tag{5}$$

δl is the differential displacement at the interface during the deforma-

tion of the composite, f is the friction between graphene and matrix, and dS is the area of slip movement. Improved interfacial bonding with coating means that Cu-coated GFs must overcome greater interfacial shear to achieve the same displacement in the metal matrix compared to uncoated GFs, thus consuming more energy.

In order to a deeper understanding variation in damping properties, the curves of loss and storage modulus with strain amplitude are analyzed. Loss modulus reflects the viscous behavior of the material, representing energy lost during deformation and proportional to tan δ. In contrast, the storage modulus indicates the elastic behavior of the material and is inversely proportional to tan δ [55]. Both Cu coating and increased GFs content result in higher loss modulus (Fig. 13), which is attributed to the sliding friction at the GFs/substrate interface that greatly contributes to energy dissipation [56]. However, at higher strain amplitudes, the loss modulus decreases for samples with high GFs content, indicating that excess GFs do not enhance energy dissipation. The storage modulus of the composites increases from 65 GPa to 77 GPa with higher GFs content, indicating improved resistance to deformation. This enhancement may stem from the high GFs content hindering dislocation motion, the primary deformation mode in metals [5]. Such hindrance leads to increased material stiffness. Additionally, adding high-modulus reinforcements to matrix allows external loads to transfer to the reinforcements, thus further increasing modulus [34]. Under the same load, materials with high GFs content experience reduced deformation and internal sliding displacements, resulting in reduced damping capacity. The gradual decrease in the storage modulus with increasing strain amplitude may arise from movement at the GFs/matrix interface and a weakening of interfacial bonding, negatively impacting mechanical properties [57]. Although the storage modulus significantly
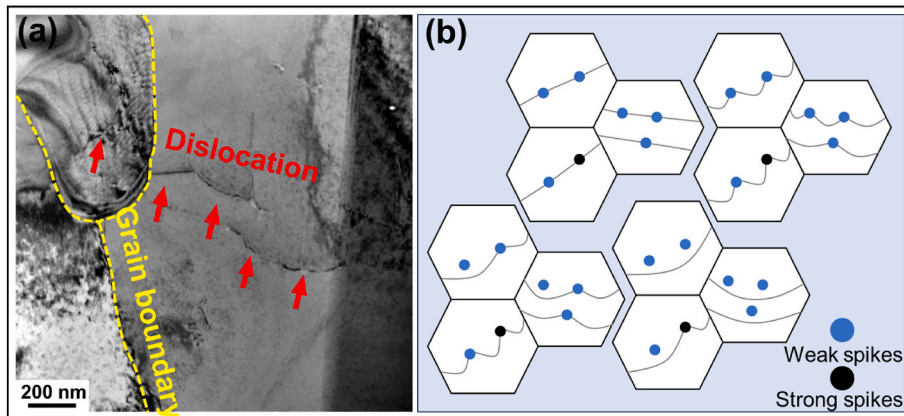

Fig. 11. (a) Dislocations in the matrix, (b) schematic diagram of dislocation damping mechanism.
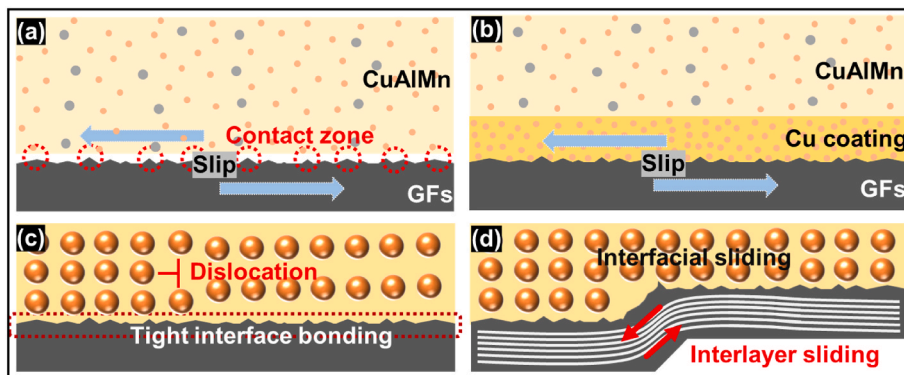

Fig. 12. Schematic diagram of interface damping: (a) Weakly bonded interfaces formed by uncoated surfaces and the presence of incomplete contact between interfaces, (b) Cu coating improves interfacial bonding and enhances wettability between graphene films and matrix, (c, d) Slip occurs at the interface as well as between graphene films layers.
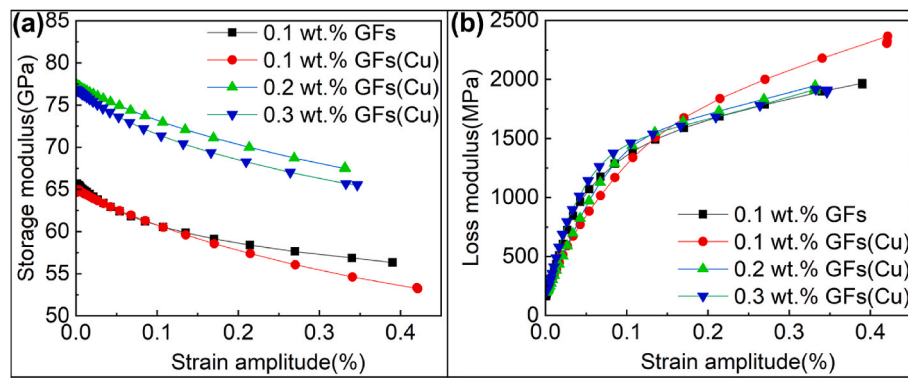
Fig. 13. Storage and loss modulus curves of the composites.

increases with GFs content, the loss modulus experiences only slight enhancement, explaining the decrease in tan δ despite the increased GFs content.

4. Conclusion

In this study, Cu particles were coated on the GFs surface by electroless plating, and bionic laminated composites were prepared by using flake powder metallurgy. The micro-morphology, mechanical properties and damping properties of the composites were characterized, and the intrinsic mechanism of Cu coating on the properties was analyzed by combining with fracture and TEM images, the following conclusions can be drawn.

1. Most of the GFs within the composites were oriented perpendicular to the compression direction, demonstrating good alignment.
2. Composite with 0.1 wt% uncoated GFs exhibited tensile strength of 338 MPa and a maximum loss factor of 0.0355. In contrast, the Cu-coated composite achieved a tensile strength of 362 MPa, and the damping properties were significantly improved with a loss factor (tan δ) of 0.044, which has an improvement of 28% compared to the uncoated sample. However, a higher content of GFs results in the decreased density and mechanical properties.
3. The improvement in tensile strength is attributed to the densified Cu coating on GFs, which creates an "interlocking effect". This effect tightly bonds GFs to the matrix, enhances interfacial shear strength, effectively inhibits dislocation movement and allows efficient load transfer.
4. The enhancement in damping properties is also due to the improved interfacial bonding of Cu coating. This bonding increases friction between GFs and the matrix, and activates interlayer slip within GFs, leading to substantial energy dissipation.

Data availability statement

The data used to support the findings of this study are available from the corresponding author upon request.

Declaration of competing interest

The authors declare that they have no known competing financial interests or personal relationships that could have appeared to influence the work reported in this paper.

Acknowledgments

References

[1] Gholami-Kermanshahi M, Wu Y-Y, Lange G, Chang S-H. Effect of alloying elements (Nb, Ag) on the damping performance of Cu–Al–Mn shape memory alloys. J Alloys Compd 2023;930:167438. https://doi.org/10.1016/j.jallcom.2022.167438.

[2] Li M, Liu J, Yan S, Yan W, Shi B. Effect of aging treatment on damping capacity in Cu–Al–Mn shape memory alloy. J Alloys Compd 2020;821:153213. https://doi.org/10.1016/j.jallcom.2019.153213.

[3] Wang QZ, Han FS, Wu J, Hao GL. Thermal stresses in a macroscopic graphite particulates reinforced CuAlMn shape memory alloy studied by internal friction. Mat Sci Eng A-Struct 2005;408(1–2):247–54. https://doi.org/10.1016/j.msea.2005.08.010.

[4] Yu Z, Yu L, Liu J. Enhancing stiffness and damping characteristics in nacreous composites through functionally graded tablet design. J Mech Behav Biomed Mater 2024;150:106242. https://doi.org/10.1016/j.jmbbm.2023.106242.

[5] Xiong DB, Cao M, Guo Q, Tan Z, Fan G, Li Z, et al. High content reduced graphene oxide reinforced copper with a bioinspired nano-laminated structure and large recoverable deformation ability. Sci Rep 2016;6:33801. https://doi.org/10.1038/srep33801.

[6] Cui S, Lu Z, Yang Z, He X. Numerical investigation on the enhanced damping behavior of bio-inspired nacreous composites by introducing interlocked structure. J Mech Behav Biomed Mater 2021;119:104442. https://doi.org/10.1016/j.jmbbm.2021.104442.

[7] Ritchie RO. The conflicts between strength and toughness. Nat Mater 2011;10(11):817–22. https://doi.org/10.1038/nmat3115.

[8] Bonderer LJ, Studart AR, Gauckler LJ. Bioinspired design and assembly of platelet reinforced polymer films. Science 2008;319(5866):1069–73. https://doi.org/10.1126/science.1148726.

[9] Walther A, Bjurhager I, Malho JM, Pere J, Ruokolainen J, Berglund LA, et al. Large-area, lightweight and thick biomimetic composites with superior material properties via fast, economic, and green pathways. Nano Lett 2010;10(8):2742–8. https://doi.org/10.1021/nl1003224.

[10] Li P, Yang M, Liu Y, Qin H, Liu J, Xu Z, et al. Continuous crystalline graphene papers with gigapascal strength by intercalation modulated plasticization. Nat Commun 2020;11(1):2645. https://doi.org/10.1038/s41467-020-16494-0.

[11] Cao M, Xiong D-B, Tan Z, Ji G, Amin-Ahmadi B, Guo Q, et al. Aligning graphene in bulk copper: nacre-inspired nanolaminated architecture coupled with in-situ processing for enhanced mechanical properties and high electrical conductivity. Carbon 2017;117:65–74. https://doi.org/10.1016/j.carbon.2017.02.089.

[12] Zhao Z, Bai P, Du W, Liu B, Pan D, Das R, et al. An overview of graphene and its derivatives reinforced metal matrix composites: preparation, properties and applications. Carbon 2020;170:302–26. https://doi.org/10.1016/j.carbon.2020.08.040.

[13] Güler Ö, Bağcı N. A short review on mechanical properties of graphene reinforced metal matrix composites. J Mater Res Technol 2020;9(3):6808–33. https://doi.org/10.1016/j.jmrt.2020.01.077.

[14] Yue H, Yao L, Gao X, Zhang S, Guo E, Zhang H, et al. Effect of ball-milling and graphene contents on the mechanical properties and fracture mechanisms of graphene nanosheets reinforced copper matrix composites. J Alloys Compd 2017;691:755–62. https://doi.org/10.1016/j.jallcom.2016.08.303.

[15] Varol T, Canakci A. The effect of type and ratio of reinforcement on the synthesis and characterization Cu-based nanocomposites by flake powder metallurgy. J Alloys Compd 2015;649:1066–74. https://doi.org/10.1016/j.jallcom.2015.07.008.

[16] Peng L, Xu Z, Liu Z, Guo Y, Li P, Gao C. Ultrahigh thermal conductive yet superflexible graphene films. Adv Mater 2017;29(27):1700589. https://doi.org/10.1002/adma.201700589.

[17] Boden A, Boerner B, Kusch P, Firkowska I, Reich S. Nanoplatelet size to control the alignment and thermal conductivity in copper-graphite composites. Nano Lett 2014;14(6):3640–4. https://doi.org/10.1021/nl501411g.

[18] Hwang J, Yoon T, Jin SH, Lee J, Kim TS, Hong SH, et al. Enhanced mechanical properties of graphene/copper nanocomposites using a molecular-level mixing process. Adv Mater 2013;25(46):6724–9. https://doi.org/10.1002/adma.201302495.

[19] Kim SY, Park HS. Multilayer friction and attachment effects on energy dissipation in graphene nanoresonators. Appl Phys Lett 2009;94(10). https://doi.org/10.1063/1.3099932.

[20] Wang C, Pan D, Chen S. Energy dissipative mechanism of graphene foam materials. Carbon 2018;132:641–50. https://doi.org/10.1016/j.carbon.2018.02.085.

[21] Ben-Shimon Y, Pradhan A, Ya'akobovitz A. Material dissipation of graphene resonators. Carbon 2023;213:118185. https://doi.org/10.1016/j.carbon.2023.118185.

[22] Lu W, Qin F, Wang Y, Luo Y, Wang H, Scarpa F, et al. Engineering graphene wrinkles for large enhancement of interlaminar friction enabled damping capability. ACS Appl Mater Interfaces 2019;11(33):30278–89. https://doi.org/10.1021/acsami.9b09393.

[23] Dorri Moghadam A, Omrani E, Menezes PL, Rohatgi PK. Mechanical and tribological properties of self-lubricating metal matrix nanocomposites reinforced by carbon nanotubes (CNTs) and graphene – a review. Compos Part B-Eng 2015;77:402–20. https://doi.org/10.1016/j.compositesb.2015.03.014.

[24] Jiang R, Zhou X, Liu Z. Electroless Ni-plated graphene for tensile strength enhancement of copper. Mat Sci Eng A-Struct 2017;679:323–8. https://doi.org/10.1016/j.msea.2016.10.029.

[25] Qamar S, Ramzan N, Aleem W. Graphene dispersion, functionalization techniques and applications: a review. Synthetic Met 2024;307:117697. https://doi.org/10.1016/j.synthmet.2024.117697.

[26] Baig Z, Mamat O, Mustapha M. Recent progress on the dispersion and the strengthening effect of carbon nanotubes and graphene-reinforced metal nanocomposites: a review. Crit Rev Solid State 2018;43(1):1–46. https://doi.org/10.1080/10408436.2016.1243089.

[27] Chu K, Wang F, Li Y-b, Wang X-h, Huang D-j, Geng Z-r. Interface and mechanical/thermal properties of graphene/copper composite with Mo2C nanoparticles grown on graphene. Compos Part A-Appl S 2018;109:267–79. https://doi.org/10.1016/j.compositesa.2018.03.014.

[28] Zhao X, Tang J, Yu F, Ye N. Preparation of graphene nanoplatelets reinforcing copper matrix composites by electrochemical deposition. J Alloys Compd 2018;766:266–73. https://doi.org/10.1016/j.jallcom.2018.06.309.

[29] Kim Y, Lee J, Yeom MS, Shin JW, Kim H, Cui Y, et al. Strengthening effect of single-atomic-layer graphene in metal-graphene nanolayered composites. Nat Commun 2013;4:2114. https://doi.org/10.1038/ncomms3114.

[30] Liu C, Jiang X, Sun H, Liu T, Wu Z, Yang L. Preparation of graphene film reinforced CoCrFeNiMn high-entropy alloy matrix composites with strength-plasticity synergy via flake powder metallurgy method. J Mater Res Technol 2023;27:7614–26. https://doi.org/10.1016/j.jmrt.2023.11.182.

[31] Schaubroeck D, Mader L, Dubruel P, Vanfleteren J. Surface modification of an epoxy resin with polyamines and polydopamine: adhesion toward electroless deposited copper. Appl Surf Sci 2015;353:238–44. https://doi.org/10.1016/j.apsusc.2015.06.114.

[32] Wang Y, Su Y, Ouyang Q, Zhu C, Cao H, Zhang D. Fabrication, mechanical and thermal properties of copper coated graphite films reinforced copper matrix laminated composites via ultrasonic-assisted electroless plating and vacuum hot-pressing sintering. Mat Sci Eng A-Struct 2021;824:141768. https://doi.org/10.1016/j.msea.2021.141768.

[33] Tang Y, Yang X, Wang R, Li M. Enhancement of the mechanical properties of graphene–copper composites with graphene–nickel hybrids. Mat Sci Eng A-Struct 2014;599:247–54. https://doi.org/10.1016/j.msea.2014.01.061.

[34] Montazeri A, Panahi B. MD-based estimates of enhanced load transfer in graphene/metal nanocomposites through Ni coating. Appl Surf Sci 2018;457:1072–80. https://doi.org/10.1016/j.apsusc.2018.07.038.

[35] Wang X, Xiao W, Wang J, Sun L, Shi J, Guo H, et al. Enhanced interfacial strength of graphene reinforced aluminum composites via X (Cu, Ni, Ti)-coating: molecular-dynamics insights. Adv Powder Technol 2021;32(7):2585–90. https://doi.org/10.1016/j.apt.2021.05.041.

[36] Han X, Huang Y, Ding L, Gao X, Xu Z. High thermal conductivity of GF@Cu@Ni/Si/Al composites reinforced with Cu and Ni co-deposited graphite flakes. Ceram Int 2020;46(11):19191–7. https://doi.org/10.1016/j.ceramint.2020.04.254.

[37] Luo F, Jiang X, Sun H, Mo D, Zhang Y, Shu R, et al. High thermal and electrical properties of electroless graphene films reinforced Cu matrix laminated composites. J Alloys Compd 2022;925:166710. https://doi.org/10.1016/j.jallcom.2022.166710.

[38] Zhang G, Yin H, Zhang C, Deng Z, Zhang R, Jiang X, et al. Effect of Mn on microstructure and properties of Cu-12Al powder metallurgy alloy. Mater Res Express 2020;7(1):016546. https://doi.org/10.1088/2053-1591/ab63f8.

[39] Zhang Y, Xu L, Zhao L, Lin D, Liu M, Qi X, et al. Process-microstructure-properties of CuAlNi shape memory alloys fabricated by laser powder bed fusion. J Mater Sci Technol 2023;152:1–15. https://doi.org/10.1016/j.jmst.2022.12.037.

[40] Cao H, Tan Z, Fan G, Guo Q, Su Y, Li Z, et al. Wide and fine alignment control and interface modification for high-performance thermally conductive graphite/copper composite. Compos Part B-Eng 2020;191:107965. https://doi.org/10.1016/j.compositesb.2020.107965.

[41] Yang L, Jiang X, Sun H, Shao Z, Fang Y, Shu R. Effects of alloying, heat treatment and nanoreinforcement on mechanical properties and damping performances of Cu–Al-based alloys: a review. Nanotechnol Rev 2021;10(1):1560–91. https://doi.org/10.1515/ntrev-2021-0101.

[42] Kim T-H, Ouyang G, Poplawsky JD, Kramer MJ, Levitas VI, Cui J, et al. In-situ TEM analysis of the phase transformation mechanism of a Cu–Al–Ni shape memory alloy. J Alloys Compd 2019;808:151743. https://doi.org/10.1016/j.jallcom.2019.151743.

[43] Liu B, Zhang D, Li X, Guo X, Shi J, Liu Z, et al. The microstructures and properties of graphite flake/copper composites with high volume fractions of graphite flake. New Carbon Mater 2020;35(1):58–65. https://doi.org/10.1016/s1872-5805(20)60475-9.

[44] Xiong K, Yang T, Sun Z, Ma C, Wang J, Ge X, et al. Modified graphene film powder scraps for re-preparation of highly thermally conductive flexible graphite heat spreaders. Carbon 2024;219:118827. https://doi.org/10.1016/j.carbon.2024.118827.

[45] Shuang F, Aifantis KE. Dislocation-graphene interactions in Cu/graphene composites and the effect of boundary conditions: a molecular dynamics study. Carbon 2021;172:50–70. https://doi.org/10.1016/j.carbon.2020.09.043.

[46] Shuang F, Aifantis KE. Modelling dislocation-graphene interactions in a BCC Fe matrix by molecular dynamics simulations and gradient plasticity theory. Appl Surf Sci 2021;535:147602. https://doi.org/10.1016/j.apsusc.2020.147602.

[47] Ebrahimi M, Zhang L, Wang Q, Zhou H, Li W. Damping performance of SiC nanoparticles reinforced magnesium matrix composites processed by cyclic extrusion and compression. J Magnesium Alloys 2023;11(5):1608–17. https://doi.org/10.1016/j.jma.2021.07.024.

[48] Madeira S, Carvalho O, Carneiro VH, Soares D, Silva FS, Miranda G. Damping capacity and dynamic modulus of hot pressed AlSi composites reinforced with different SiC particle sized. Compos Part B-Eng 2016;90:399–405. https://doi.org/10.1016/j.compositesb.2016.01.008.

[49] Yang G, Han Y, Lu A, Guo Q. Enhanced damping capacity of nanolaminated graphene (reduced graphene oxide)/Al-Mg-Si composite. Compos Part A-Appl S 2022;156:106887. https://doi.org/10.1016/j.compositesa.2022.106887.

[50] Gu J, Zhang X, Qiu Y, Gu M. Damping behaviors of magnesium matrix composites reinforced with Cu-coated and uncoated SiC particulates. Compos Sci Technol 2005;65(11–12):1736–42. https://doi.org/10.1016/j.compscitech.2005.02.014.

[51] Liu G, Tang S, Ren W, Hu J, Li D. Damping peak and damping mechanism in Al18B4O33w/Al composite containing Sn and Bi interfacial phases at room temperature. Mater Des 2013;46:916–21. https://doi.org/10.1016/j.matdes.2012.11.045.

[52] Peng Y, Luo G, Hu Y, Xiong DB. Dynamic deformation mechanism in submicro-laminated copper with interlamellar graphene multilayers. Acta Mater 2023;252:118941. https://doi.org/10.1016/j.actamat.2023.118941.

[53] Gong L, Zhang F, Peng X, Scarpa F, Huang Z, Tao G, et al. Improving the damping properties of carbon fiber reinforced polymer composites by interfacial sliding of oriented multilayer graphene oxide. Compos Sci Technol 2022;224:109309. https://doi.org/10.1016/j.compscitech.2022.109309.

[54] Feng J, Safaei B, Qin Z, Chu F. Effects of graphene surface morphology on damping properties of epoxy composites. Polymer 2023;281:126107. https://doi.org/10.1016/j.polymer.2023.126107.

[55] Sujon MAS, Masato D, Andriollo T, Pan Z, Nadimpalli VK, Henriquez VC, et al. Novel approach for optimizing mechanical and damping performance of MABS composites reinforced with basalt fibers: an experimental study. Compos Sci Technol 2024;251:110578. https://doi.org/10.1016/j.compscitech.2024.110578.

[56] Jiang Z, Cai H, Chen X, Gong S, Liu D, Pang Y, et al. Improving the mechanical and damping properties of polymer/memory alloy composite by introducing nanotubes covered with nano-scale Ni particles. Compos Part A-Appl S 2022;156:106856. https://doi.org/10.1016/j.compositesa.2022.106856.

[57] Feng J, Safaei B, Qin Z, Chu F. Nature-inspired energy dissipation sandwich composites reinforced with high-friction graphene. Compos Sci Technol 2023;233:109925. https://doi.org/10.1016/j.compscitech.2023.109925.